

Gate-controlled proximity magnetoresistance in $\text{In}_{1-x}\text{Ga}_x\text{As}/(\text{Ga,Fe})\text{Sb}$ bilayer heterostructuresKosuke Takiguchi,¹ Kyosuke Okamura,¹ Le Duc Anh ^{1,2,3,4,*} and Masaaki Tanaka ^{1,4,5,†}¹*Department of Electrical Engineering and Information Systems, The University of Tokyo, Bunkyo-ku, Tokyo 113-8656, Japan*²*Institute of Engineering Innovation, The University of Tokyo, Bunkyo-ku, Tokyo 113-8656, Japan*³*PRESTO, Japan Science and Technology Agency, Kawaguchi, Saitama 332-0012, Japan*⁴*Center for Spintronics Research Network (CSRN), The University of Tokyo, Bunkyo-ku, Tokyo 113-8656, Japan*⁵*Institute for Nano Quantum Information Electronics, The University of Tokyo, 4-6-1, Komaba, Meguro-ku, Tokyo 153-8505, Japan* (Received 15 December 2021; revised 10 May 2022; accepted 11 May 2022; published 21 June 2022)

The magnetic proximity effect (MPE), ferromagnetic (FM) coupling at the interface of magnetically dissimilar layers, has attracted much attention as a promising pathway for introducing ferromagnetism into a high-mobility nonmagnetic (NM) conducting channel. Recently, our group found giant proximity magnetoresistance (PMR), which is caused by MPE at an interface between a NM semiconductor InAs quantum well (QW) layer and a FM semiconductor (Ga,Fe)Sb layer. The MPE in the NM semiconductor can be modulated by applying a gate voltage and controlling the penetration of the electron wave function in the InAs QW into the neighboring insulating FM (Ga,Fe)Sb layer. However, optimal conditions to obtain strong MPE at the InAs/(Ga,Fe)Sb interface have not been clarified. In this paper, we systematically investigate the PMR properties of $\text{In}_{1-x}\text{Ga}_x\text{As}$ ($x = 0, 5, 7.5,$ and 10%)/(Ga,Fe)Sb bilayer semiconductor heterostructures under a wide range of gate voltage. The inclusion of Ga alters the electronic structures of the InAs thin film, changing the effective mass and the QW potential of electron carriers. Our experimental results and theoretical analysis of the PMR in these $\text{In}_{1-x}\text{Ga}_x\text{As}/(\text{Ga,Fe})\text{Sb}$ heterostructures show that the MPE depends not only on the degree of penetration of the electron wave function into (Ga,Fe)Sb but also on the electron density. These findings help us to unveil the microscopic mechanism of MPE in semiconductor-based NM/FM heterojunctions.

DOI: [10.1103/PhysRevB.105.235202](https://doi.org/10.1103/PhysRevB.105.235202)**I. INTRODUCTION**

Introducing a ferromagnetic (FM) coupling into a high-mobility semiconducting channel can lead to spintronics devices with nonvolatile and reconfigurable functions. One straightforward method toward this goal is doping magnetic impurities into a nonmagnetic (NM) semiconductor, which led to the creation of FM semiconductors (FMSs), such as (III,TM)V, where TM is a transition metal element (Mn, Fe). However, carrier transport in FMSs is subject to frequent scatterings by magnetic impurities; thus, the carrier mobility is very low ($\sim 1\text{--}10\text{ cm}^2/\text{Vs}$). For electronic device applications, it is important to obtain large magnetic responses in NM channels with high carrier mobility, minimizing scatterings by magnetic impurities. Utilizing a magnetic proximity effect (MPE), which is a magnetic coupling at magnetically dissimilar layers, is one of the most promising pathways for this purpose [1–7]. Bilayer systems consisting of a NM conductive channel and a FM insulator (FMI) hold a magnetic coupling via MPE at the interface. In addition, since these bilayer systems have only one FM layer, the device fabrication is much simpler than that in the conventional spin-valve structures which contain FM/NM/FM trilayer and more complicated multilayer structures [8–11]. Therefore, the

magnetotransport phenomena induced by MPE in the FM/NM bilayers have been actively studied in metallic systems in recent years [12–21]. (See also Table S1 in the Supplemental Material [22].) Notable examples of magnetoresistance (MR) in bilayer systems are spin Hall MR (SMR) [12,13,16–18,21] and unidirectional SMR (USMR) [14,15,19,20]. These phenomena pave ways to manipulate the electrical transport in a NM channel by the magnetization of a neighboring FM layer. However, at these metallic NM/FM interfaces [12–18], the MR magnitude is too small ($< 0.1\text{--}1\%$) for practical purposes, which is mainly due to the short-range nature of the magnetic coupling ($< 1\text{ nm}$). Recently, relatively large MR magnitude ($< 30\%$) has been reported only in exotic materials such as $(\text{Bi,Sb})_2\text{Te}_3/\text{Cr-doped } (\text{Bi,Sb})_2\text{Te}_3$, which possess a strong spin-momentum locking effect in the topological edge state [19,20].

In contrast, *semiconductor-based* NM/FM bilayer systems can overcome the problem of the metallic counterparts because the higher coherency and smaller concentration of carriers enhance the interfacial magnetic coupling range. When we prepare a NM semiconducting quantum well (QW) interfaced with an insulating FM layer, as shown in Fig. 1(a), even small penetration of the wave function of a two-dimensional (2D) carrier in the QW into the neighboring FMS layer is enough to yield a strong MPE. This is because the 2D carrier system feels the spin-carrier interactions occurring at the interface as a whole, due to their high coherency. Furthermore, the MPE can be modulated by an external gate voltage,

*anh@cryst.t.u-tokyo.ac.jp

†masaaki@ee.t.u-tokyo.ac.jp

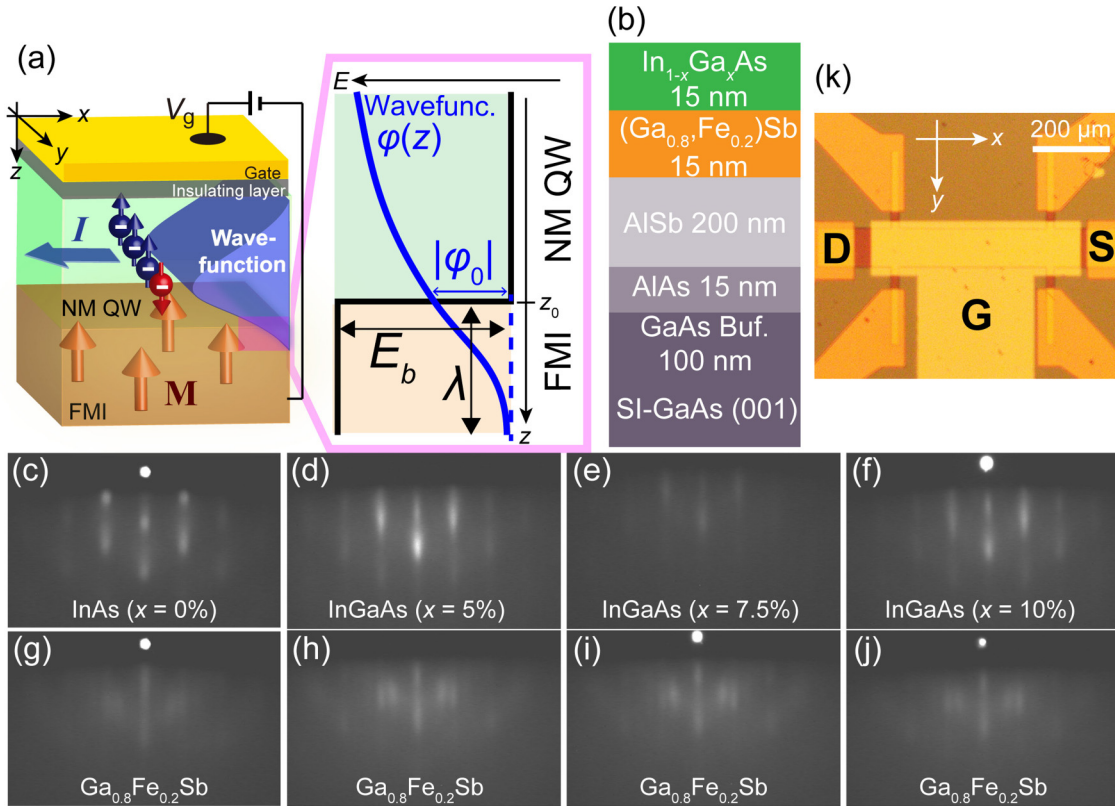


FIG. 1. (a) Schematic (left) device structure and (right) band alignment with electron carrier wave function (blue curve) in a nonmagnetic (NM) quantum well (QW)/ferromagnetic (FM) insulator (FMI) heterostructure. In the left image, the wave function in the NM QW penetrates the FMI. When an electrical current I flows in the in-plane direction, electrons interact with the neighboring magnetization M at the interface and are partially magnetized by magnetic proximity effect (MPE). A semiconductor-based NM/FM bilayer system enables modulation of the MPE by controlling the wave function with a top gate voltage V_g . In the right image, the black solid line indicates the conduction band bottom of both materials. The carrier wave function penetrates the FMI side with a penetration depth λ , determined by the barrier height E_b and the wave function amplitude at the interface $|\varphi_0|$. (b) Sample structure of D_0 , D_5 , $D_{7.5}$, and D_{10} with $x = 0, 5, 7.5$, and 10% , respectively. (c)–(f) Reflection high-energy electron diffraction (RHEED) patterns of $\text{In}_{1-x}\text{Ga}_x\text{As}$ and (g)–(j) those of $(\text{Ga,Fe})\text{Sb}$ during the MBE growth of $\text{In}_{1-x}\text{Ga}_x\text{As}/(\text{Ga,Fe})\text{Sb}$ heterostructures with $x = 0, 5, 7.5$, and 10% , respectively. (k) Top-view optical microscopy image of a field-effect transistor (FET) device ($x = 5\%$, D_5) examined in this paper. We apply an electron current from the source (S) to the drain (D) and a gate voltage V_g from the gate electrode (G) to S.

which enhances the penetration by pushing the wave function toward the FM side. Therefore, the spin-splitting energy induced by MPE can be controlled by external electrical means.

Recently, we demonstrated this advantage of the semiconductor NM/FM bilayer systems using NM InAs QW/FM $(\text{Ga,Fe})\text{Sb}$ heterostructures [23]. The InAs/ $(\text{Ga,Fe})\text{Sb}$ bilayer heterostructures have distinct merits as follows: (i) $(\text{Ga,Fe})\text{Sb}$ is a p -type FMS with high Curie temperature >300 K [24,25]. (ii) The lattice mismatch between InAs and $(\text{Ga,Fe})\text{Sb}$ is only of the order of 0.1% , which allows epitaxial growth of high-quality single-crystalline heterostructures. (iii) InAs/ $(\text{Ga,Fe})\text{Sb}$ has a type-III band lineup, in which the bottom of the conduction band of InAs is lower than the top of the valence band of $(\text{Ga,Fe})\text{Sb}$ at the NM/FM interface. This leads to large penetration of the electron wave function of the InAs QW into the $(\text{Ga,Fe})\text{Sb}$ side. (iv) At low temperature (<5 K), the resistivity of $(\text{Ga,Fe})\text{Sb}$ is two-orders of magnitude higher than that of the InAs QW; thus, electron carriers mainly flow into the InAs QW. The strong MPE led to the discovery of a proximity MR (PMR), whose magnitude reaches 20% at 10

T, which is 20-fold larger than that of metallic systems, and a large spontaneous spin-splitting energy (~ 3.8 meV) in the InAs QW. Moreover, we successfully enhanced the PMR by applying a gate voltage.

However, to fully control the properties of the InAs/ $(\text{Ga,Fe})\text{Sb}$ heterostructures and to realize practical spintronic applications, it is essential to obtain deeper insights into the microscopic mechanism of the MPE. To quantitatively estimate the MPE and spontaneous spin-splitting energy induced in the NM channel, which is practically important, there are four main parameters that can be controlled experimentally: The penetration P of the electron wave function of the NM QW channel into the FM side, the electron concentration n , the barrier height E_b , and the effective mass m^* of the electron carriers in the NM QW. These four parameters are closely correlated. As shown in Fig. 1(a), the wave function $\varphi(z)$ decays exponentially in the FMI; $\varphi(z) = |\varphi_0| \exp[-(z - z_0)/\lambda]$, where $|\varphi_0|$ is the amplitude of the wave function at the interface, z is the axis in the growth direction, and z_0 is the position at the interface of NM/FM.

Then the penetration P is given by $P = |\varphi_0|\lambda$. According to the Wentzel-Kramers-Brillouin approximation [26–28] for tunnelling phenomena, $\lambda \propto 1/\sqrt{E_b}$ and $|\varphi_0| \propto (m^*)^{-1/4}$. Thus, large E_b and/or m^* suppress P and consequently the MPE. Larger n also leads to heavier m^* due to the nonparabolicity of the InAs conduction band and suppresses the MPE [29,30]. On the other hand, an important question is whether larger n can induce stronger MPE or not via enhancement of the interfacial s - d exchange coupling between electron carriers and Fe spins in the FMS, a well-known effect in conventional carrier-induced FMSs [31]. Therefore, to obtain larger spin-splitting energy ΔE via MPE, investigating how ΔE depends on these tradeoff parameters is crucial for seeking the optimal conditions.

In this paper, we investigate the PMR phenomena in field-effect transistor (FET) structures of $\text{In}_{1-x}\text{Ga}_x\text{As}$ ($x = 0, 5, 7.5, \text{ and } 10\%$)/ $(\text{Ga,Fe})\text{Sb}$ bilayers while applying a top gate voltage V_g . Compared with the previous study of PMR in $\text{InAs}/(\text{Ga,Fe})\text{Sb}$ [23], Ga inclusion in the InAs channel (In-GaAs channel) changes the E_b and m^* , which affects the penetration P . By the analysis of the PMR observed in these four samples, we find that ΔE depends on n and the momentum relaxation time τ of electron carriers. These results suggest that ΔE is almost proportional to n in an accumulation state of the FET operation, which indicates that the spin splitting via MPE is induced not only by the penetration P of the wave function but also by the large carrier density n .

II. EXPERIMENT

We grew heterostructures consisting of $\text{In}_{1-x}\text{Ga}_x\text{As}$ (15 nm, $x = 0, 5, 7.5, \text{ and } 10\%$)/ $(\text{Ga,Fe})\text{Sb}$ (15 nm, Fe 20%)/AlSb (140 nm)/AlAs (10 nm)/GaAs (100 nm) on semi-insulating GaAs (001) substrates by molecular beam epitaxy (MBE) [Fig. 1(b)]. The growth temperature was 550 °C for the GaAs and AlAs layers, 470 °C for the AlSb layer, and 250 °C for the $(\text{Ga,Fe})\text{Sb}$ and $\text{In}_{1-x}\text{Ga}_x\text{As}$ layers. The Ga content ($= x$) was determined by the ratio of In and Ga fluxes, which were calibrated using reflection high-energy electron diffraction (RHEED) intensity oscillations. *In situ* RHEED patterns of the $\text{In}_{1-x}\text{Ga}_x\text{As}$ [Figs. 1(c)–1(f)] and $(\text{Ga,Fe})\text{Sb}$ [Figs. 1(g)–1(j)] layers were bright and streaky, indicating good crystal quality and smooth surface during the growth.

We first patterned the samples into 100 μm (width) \times 400 μm (length) Hall bars using standard photolithography and Ar ion milling and then formed several electrodes [source (S), drain (D), and electrodes for transport measurements] using sputtering deposition and lift-off of an Au (50 nm)/Cr (5 nm) film. An insulating Al_2O_3 layer (~ 50 nm) was deposited as a gate insulator at 170 °C on the Hall bars using atomic layer deposition (ALD). It is known that depositing Al_2O_3 using ALD can decrease the interfacial state density at the $\text{In}_{1-x}\text{Ga}_x\text{As}/\text{oxide}$ interface [32,33]. Thus, it is expected that the modulation of the electrical properties by the gate voltage in our $\text{Al}_2\text{O}_3/\text{In}_{1-x}\text{Ga}_x\text{As}/(\text{Ga,Fe})\text{Sb}$ FETs is more effective than that of the $\text{HfO}_2/\text{InAs}/(\text{Ga,Fe})\text{Sb}$ FETs reported in our previous study of PMR [23]. Finally, we formed a top-gate electrode (G), again by sputtering deposition and lift-off processes of an Au (50 nm)/Cr (5 nm) film. Figure 1(k) shows an optical microscope image of the FET device examined in

this paper. We applied a gate voltage V_g between the G and S electrodes. We measured the longitudinal resistance R_{xx} by a standard four-terminal method and the Hall resistance R_{xy} simultaneously at 3.5 K. In this paper, a magnetic field B was always applied perpendicular to the film plane. In our recent study on the magnetotransport properties of $\text{InAs}/(\text{Ga,Fe})\text{Sb}$ bilayers, we have found a type of odd-parity MR (OMR), which is an odd function against B , and the resistance change reaches almost 13.5% of the total resistance at 10 T [34]. Although the OMR is also observed here, this phenomenon is out of the scope of this paper and will be discussed elsewhere. Therefore, all the MR and the Hall resistance data in this paper were obtained by extracting only the even- and odd-function components against B from the raw data, respectively. To evaluate the transport properties of the $(\text{Ga,Fe})\text{Sb}$ layer, we etched the top $\text{In}_{1-x}\text{Ga}_x\text{As}$ layer in one sample ($x = 7.5\%$, device $\text{D}_{7.5}$), and measured the resistivity of the remaining $(\text{Ga,Fe})\text{Sb}$ layer at 3.5 K (see Table S2 in the Supplemental Material [22]). The resistivity of the $(\text{Ga,Fe})\text{Sb}$ layer is >100 times larger than that of the $\text{In}_{1-x}\text{Ga}_x\text{As}$ layer ($x = 0, 5, 7.5, \text{ and } 10\%$), which indicates that the conduction in the $\text{In}_{1-x}\text{Ga}_x\text{As}$ layer dominates the whole transport. To obtain the QW potential and electron carrier wave functions in the $\text{In}_{1-x}\text{Ga}_x\text{As}$ channel, we performed a self-consistent calculation for the case of $x = 5\%$ using Nextnano3. We note that the Fermi level in this calculation was assumed to be pinned at 0.60 eV below the conduction band bottom of $(\text{Ga,Fe})\text{Sb}$ due to the Fe impurity band in the bandgap of this FMS, as estimated in our previous study [35].

III. RESULTS AND DISCUSSIONS

Figure 2(a)–2(d) show the MR data of $\text{In}_{1-x}\text{Ga}_x\text{As}$ ($x = 0, 5, 7.5, \text{ and } 10\%$)/ $(\text{Ga,Fe})\text{Sb}$ FET devices, named $\text{D}_0, \text{D}_5, \text{D}_{7.5}, \text{ and } \text{D}_{10}$, respectively, with a wide range of V_g ($-10 \text{ V} < V_g < 10 \text{ V}$). As summarized in Fig. 3(a), the MRs at 1 T $\{= [R_{xx}(B = 1 \text{ T}) - R_{xx}(0 \text{ T})]/R_{xx}(0 \text{ T})\}$ in $\text{D}_0, \text{D}_5, \text{ and } \text{D}_{10}$ show a systematic change from negative to positive when negative V_g is applied from 0 to -10 V. In $\text{D}_{7.5}$, the negative MR is suppressed to nearly zero at $V_g = -8$ V. This variation of PMR can be understood by contributions of both Kondo scattering and s - d exchange interaction at the NM/FM interface, as will be explained later. Also, the x dependence of the MR magnitude at $V_g = 0$ V can be understood by the variation of E_b and m^* at different x values (see the Supplemental Material [22]).

We fit a modified Khosla-Fischer model [23,36] using the following equations [Eqs. (1)–(5)] to our experimental results shown in Figs. 2(a)–2(d). We found that this model excellently describes the magnetotransport results in the NM $\text{In}_{1-x}\text{Ga}_x\text{As}$ channels with MPE:

$$\frac{\Delta\rho}{\rho} = -a^2 \ln(1 + b^2 H^2) + \frac{c^2 H^2}{1 + d^2 H^2}, \quad (1)$$

where

$$a = A_1 J D(\epsilon_F) [S(S + 1) + \langle M^2 \rangle], \quad (2)$$

$$b^2 = \left[1 + 4S^2 \pi^2 \left(\frac{2JD(\epsilon_F)}{g} \right)^4 \right] \left(\frac{g\mu_B}{\alpha k_B T} \right)^2, \quad (3)$$

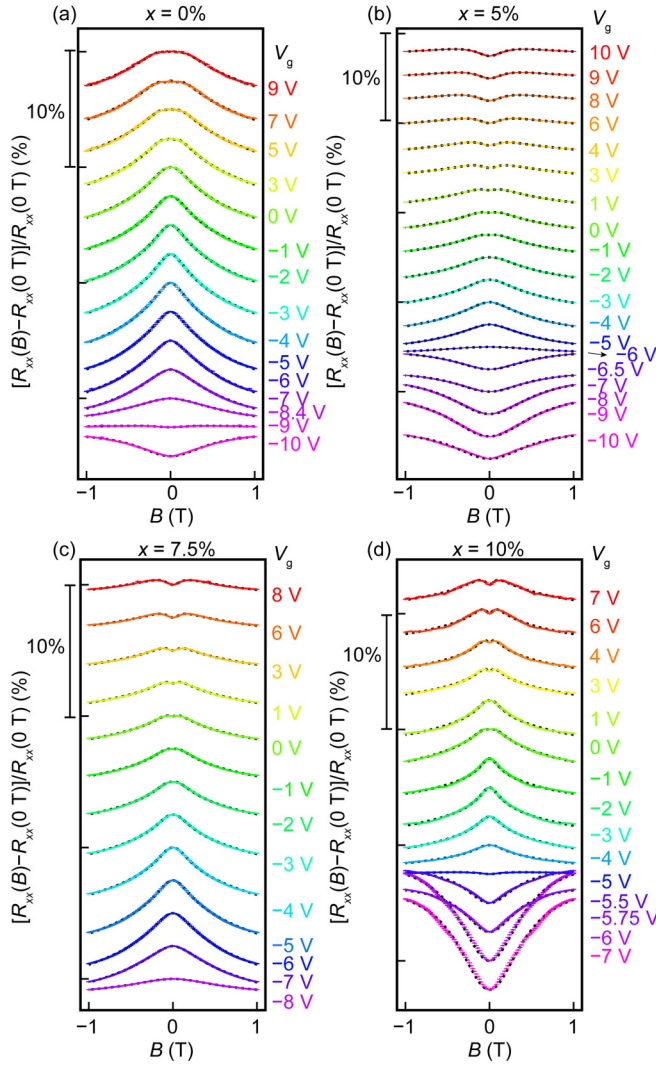


FIG. 2. (a)–(d) Magnetoresistance (MR) $\{[R_{xx}(B) - R_{xx}(0 T)]/R_{xx}(0 T)\}$ of the $\text{In}_{1-x}\text{Ga}_x\text{As}/(\text{Ga,Fe})\text{Sb}$ heterostructures with $x = 0, 5, 7.5,$ and 10% under various V_g with a perpendicular magnetic field B ($\parallel[001]$ of GaAs substrate) at 3.5 K, respectively. The black dashed curves represent the fitting results from Eq. (1). The MR curves of $x = 0, 5, 7.5,$ and 10% at each V_g have been offset by 2.5% for a clearer view. The error bars are estimated by voltage accuracy ($\pm 0.5\%$) of each measurement point in our lock-in amplifier. As the error bar is $< 0.1\%$, most of the error bars are too small to be visible in the graphs.

$$c^2 = \frac{\sigma_1\sigma_2(\mu_1 + \mu_2)^2}{(\sigma_1 + \sigma_2)^2}, \quad (4)$$

$$d^2 = \frac{(\sigma_1\mu_2 - \sigma_2\mu_1)^2}{(\sigma_1 + \sigma_2)^2}. \quad (5)$$

In Eqs. (2) and (3), A_1 is a constant representing the contribution of spin scattering to the whole MR, α is a numerical factor that is on the order of unity, $D(E_F)$ is the density of states at the Fermi level E_F , g is the effective Lande factor of the $\text{In}_{1-x}\text{Ga}_x\text{As}$ QW, $\langle M^2 \rangle$ is the averaged squared magnetization, S is the localized spin moment of (Ga,Fe)Sb [we

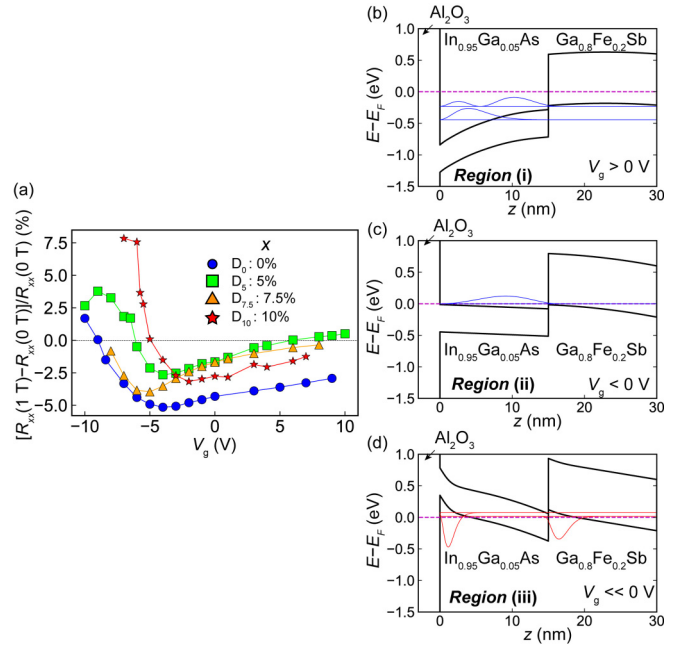


FIG. 3. V_g dependence of the magnetoresistance (MR) ratio at 1 T $\{=[R_{xx}(1 T) - R_{xx}(0 T)]/R_{xx}(0 T)\}$ in all devices examined in this paper. Blue circles, green squares, orange triangles, and red stars indicate the data of devices $D_0, D_5, D_{7.5},$ and D_{10} , respectively. (b)–(d) Self-consistent calculation results of the band profile in device D_5 ($x = 5\%$) in the growth direction (z). The blue and red curves indicate the electron and hole wave functions in accumulation [(b) $V_g > 0$ V, region (i)], depletion [(c) $V_g < 0$ V, region (ii)], and inversion [(d) $V_g \ll 0$ V, region (iii)] operation, respectively. Purple dashed line indicates the Fermi level E_F .

assume $S = \frac{5}{2}$ for Fe^{3+} ions in (Ga,Fe)Sb], and J is the $s,p-d$ exchange interaction energy at the NM/FM bilayer interface. In Eqs. (4) and (5), σ_i and μ_i represent the conductivity and mobility of electron carriers in $\text{In}_{1-x}\text{Ga}_x\text{As}$, respectively. The subscripts 1 and 2 of each parameter denote the majority and minority spins, respectively. The first term on the right side of Eq. (1), which gives a negative MR component, is due to the Kondo scattering of electron carriers in the $\text{In}_{1-x}\text{Ga}_x\text{As}$ by the localized Fe spins at the (Ga,Fe)Sb interface. The second term on the right side of Eq. (1), which gives a positive MR component, is caused by the $s-d$ exchange interaction between transport carriers in $\text{In}_{1-x}\text{Ga}_x\text{As}$ and the localized Fe spins at the interface of $\text{In}_{1-x}\text{Ga}_x\text{As}/(\text{Ga,Fe})\text{Sb}$. The fitting results using Eq. (1) are shown by black dashed curves in Figs. 2(a)–2(d), showing excellent agreement with the experimental MR curves at various V_g .

From the modified Khosla-Fischer model of Eq. (1), the interesting behavior of the PMR in our samples can be understood as follows: The negative MR component, which is induced by the Kondo effect, is enhanced under large penetration P of the electron carrier wave function into the FMS (Ga,Fe)Sb, as we experimentally proved in the previous work [23]. Considering the FET operation with a 2D electron gas channel in the $\text{In}_{1-x}\text{Ga}_x\text{As}$ QW, there are three different regions of the PMR depending on the gate voltage V_g , as shown in Figs. 3(b)–3(d): [(i), accumulation region] As shown in

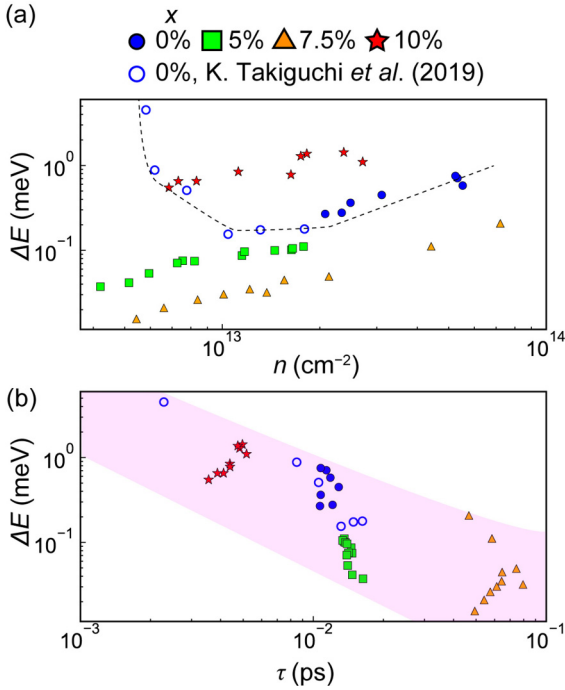


FIG. 4. (a) Spin splitting ΔE vs electron concentration n and (b) relaxation time τ of devices D_0 (blue circles), D_5 (green squares), $D_{7.5}$ (orange triangles), and D_{10} (red stars). Blue open circles are for device \tilde{D}_0 [21]. Black dashed line in (a) is an eye guide for a clear view of the InAs/(Ga,Fe)Sb data. The pink shaded area in (b) represents the eye guide for the negative correlation of ΔE vs τ .

Fig. 3(b), when a positive or zero V_g is applied, the wave function is shifted toward the Al_2O_3 layer side, and the penetration of the electron wave function into the (Ga,Fe)Sb side is small but not zero. Therefore, the PMR shows small negative MR. In this region, the electron carrier concentration n is larger than other regions. [(ii), depletion region] As shown in Fig. 3(c), when a small negative V_g is applied, the carrier wave function in the $\text{In}_{1-x}\text{Ga}_x\text{As}$ QW is pushed toward the FM (Ga,Fe)Sb side, which leads to the larger negative MR. The electron carrier concentration n is smaller than that in (i). [(iii), inversion region] As shown in Fig. 3(d), when a large negative V_g is applied, the channel is eventually inverted, and hole carriers are induced at the $\text{Al}_2\text{O}_3/\text{In}_{1-x}\text{Ga}_x\text{As}$ interface far from the FMS side. These hole carriers do not interact with the magnetic moments in the (Ga,Fe)Sb layer, and thus, MPE is again suppressed. Also, our calculation suggests that there are holes accumulated in the (Ga,Fe)Sb layer near the InAs/(Ga,Fe)Sb interface, which may lead to nonlinear magnetic field dependence in the Hall resistance (see the Supplemental Material [22]). As the region goes close to (iii), the PMR should be decreased. Therefore, when the V_g becomes more negative to enhance the penetration, the electrons are fully depleted eventually at negative large V_g , and there is no MPE at all. In other words, appropriate V_g should be chosen to obtain the largest spin splitting ΔE .

Next, we discuss the dependence of ΔE on n and τ ($= \mu_n m^*/e$, μ_n is electron mobility), the data of which are shown in Figs. 4(a) and 4(b), respectively. Here, ΔE in a 2D electron system is estimated from the modified Khosla-Fischer model

[23,36]:

$$\Delta E = 2\pi\hbar^2 \frac{n}{\mu_n m^*} d = \frac{2\pi\hbar^2}{e} \frac{n}{\tau} d, \quad (6)$$

where d is the fitting parameter from Eq. (5), and n and μ_n are estimated from the ordinary Hall effect measurements (detailed discussions on the Hall effect data and analyses on $\text{In}_{1-x}\text{Ga}_x\text{As}/(\text{Ga,Fe})\text{Sb}$ are described in the Supplemental Material [22], and see also Refs. [37–39] therein). Here, m^* of $\text{In}_{1-x}\text{Ga}_x\text{As}$, m_{InGaAs}^* , is determined by a linear interpolation between the effective mass of InAs (m_{InAs}) and GaAs (m_{GaAs}), taken from the literature: $m_{\text{In}_{1-x}\text{Ga}_x\text{As}}^*(x, n) = m_{\text{InAs}/(\text{Ga,Fe})\text{Sb}} + x[m_{\text{GaAs}}(n) - m_{\text{InAs}}(n)]$ [29,40], where $m_{\text{InAs}/(\text{Ga,Fe})\text{Sb}}$ is obtained by our recent study of Shubnikov–de Haas (SdH) oscillations in InAs/(Ga,Fe)Sb [41]. We have recently found that $m_{\text{InAs}/(\text{Ga,Fe})\text{Sb}}$ does not strongly depend on n , which is different from that in a NM InAs QW. In a usual NM InAs, m^* increases with increasing n because of the nonparabolicity of the InAs conduction band. However, in the present case of InAs/(Ga,Fe)Sb bilayers, when we apply a positive gate voltage V_g , n is increased (making m^* heavier), but P is decreased (making m^* lighter due to the smaller s - d exchange interaction at the NM/FM interface). Thus, it is reasonable that m^* only weakly depends on n , as observed experimentally [31]. According to Eq. (6), this result suggests that n and τ significantly affect the spin-splitting ΔE .

Figure 4(a) shows the n dependence of ΔE in all the FET devices (D_0 , D_5 , $D_{7.5}$, and D_{10} ; solid circles, squares, triangles and stars, respectively), comparing with the previous result in InAs/(Ga,Fe)Sb (\tilde{D}_0 ; open circles) [23]. Note that \tilde{D}_0 has a same semiconductor heterostructure as D_0 , and we re-estimate ΔE of the previous study in \tilde{D}_0 [23] by considering the n dependence of m^* . At first, we found that, unlike device \tilde{D}_0 in the previous work, ΔE of devices D_0 , D_5 , $D_{7.5}$, and D_{10} increases with increasing n . In two devices, \tilde{D}_0 and D_0 , both contain an InAs channel ($x = 0$), the ΔE – n relationship shows a U-shaped curve, where ΔE first decreases at $n < 1 \times 10^{13} \text{ cm}^{-2}$ (in device \tilde{D}_0) but increases at higher $n > 2 \times 10^{13} \text{ cm}^{-2}$ (in device D_0) as n increases. These results clearly indicate a general trend that the MPE is enhanced at larger n when increasing n above a specific threshold value. This can be explained by two counteracting effects of the gate voltage V_g on the MPE in our FET devices: The electron wave function penetration (P)- and electron concentration (n)-induced effects. In the region with small n [corresponding to region (ii) at negative V_g], P is large, and the penetration-induced effect dominates the MPE. An increase of V_g toward the positive side decreases P and thus suppresses MPE. At large positive V_g [corresponding to region (i)], while the penetration P is minimized, a larger n enhances the s - d exchange interaction at the InAs/(Ga,Fe)Sb interface, as commonly observed in carrier-induced FMSs. Thus, the carrier-induced effect becomes more prominent, leading to stronger MPE and a larger spin splitting at the large- n region. These results clarify the important roles of both factors, the electron concentration n and the penetration P of the electron wave function, for increasing the MPE and ΔE .

We note that the ΔE – n relationships in devices D_5 , $D_{7.5}$, and D_{10} do not show an increase of ΔE in the low- n

region, whereas device \tilde{D}_0 shows an increase of ΔE in the low- n region due to the P -induced MPE. This is because adding Ga into the InAs film and increasing the Ga content x in $\text{In}_{1-x}\text{Ga}_x\text{As}$ increase the effective mass m^* of electron carriers, which leads to smaller electron wave function penetration P into (Ga,Fe)Sb. Therefore, one needs to apply a larger negative V_g (corresponding to smaller n) to see the same enhancement of ΔE at low n in the devices (D_5 , $D_{7.5}$, and D_{10}) with an InGaAs channel. This, unfortunately, is unavailable in our present experiments. Comparing with the case of device \tilde{D}_0 , all the FET channels in devices D_0 , D_5 , $D_{7.5}$, and D_{10} quickly reach the inversion region (iii) at negative V_g , where holes are increased, and parallel conduction occurs (see also the Supplemental Material [22]). The difference might originate from the weaker pinning effect of the Fermi level in the $\text{Al}_2\text{O}_3/\text{In}_{1-x}\text{Ga}_x\text{As}/(\text{Ga, Fe})\text{Sb}$ FETs than that in the $\text{HfO}_2/\text{InAs}/(\text{Ga, Fe})\text{Sb}$ FETs in the previous work [23]. The Khosla-Fischer model, which is only available when the conduction occurs in a single channel, is thus unable to be used to estimate ΔE in the low- n region [$n < 5 \times 10^{12} \text{ cm}^{-2}$; there may be a parallel conduction of a hole channel, as shown in Fig. 3(d)] in devices D_0 , D_5 , $D_{7.5}$, and D_{10} . Further studies are required to determine ΔE in the NM channel in the low- n region without using Hall resistance data. For example, observing the spin-split Fermi surface using SdH oscillations is a promising approach, which will be reported elsewhere [41].

Finally, we comment on the $\Delta E - \tau$ relationship shown in Fig. 4(b). Comparing all the data shown in Fig. 4(b), it is found that ΔE increases with decreasing τ . From the modified Khosla-Fischer model, larger penetration P of the carrier wave function of the NM channel into the (Ga,Fe)Sb side, which enhances ΔE , leads to larger spin-dependent scattering for the carriers and results in smaller τ . Therefore, the negative correlation between ΔE and τ can be reasonably understood.

IV. CONCLUSIONS

In conclusion, we investigate the MPE in semiconductor NM/FM heterostructures by characterizing the magnetotransport properties of $\text{In}_{1-x}\text{Ga}_x\text{As}/(\text{Ga,Fe})\text{Sb}$ heterostructures. We performed the systematic analysis of the MPE by measuring the gate-controlled PMR using standard FET operation. These results clearly indicate a general trend that the $\Delta E - n$ characteristics follow a U shape, and the MPE is enhanced at larger n when increasing n above a specific threshold value. From the $\Delta E - n$ characteristics, there are two counteracting effects that affect the ΔE : One is determined by the electron concentration which leads to carrier-induced s - d exchange interaction at the NM/FM interface, and the other is determined by the penetration depth of the electron wave function into the FM side. Therefore, to obtain large MPE, to choose the appropriate carrier concentration is crucial. The data obtained in this paper will play an important role in unveiling the microscopic mechanism of MPE in semiconductor-based NM/FM heterostructures.

The data that support the findings of this paper are available from the corresponding author upon reasonable request.

ACKNOWLEDGMENTS

This paper was partly supported by Grants-in-Aid for Scientific Research (No. 18H05345, No. 20H05650, No. 20K15163, and No. 20H02196), the CREST (No. JPMJCR1777) and PRESTO (No. JPMJPR19LB) Programs of JST, and the Spintronics Research Network of Japan (Spin-RNJ). A part of this paper was conducted at the Advanced Characterization Nanotechnology Platform of the University of Tokyo, supported by the Nanotechnology Platform of the Ministry of Education, Culture, Sports, Science and Technology, Japan.

-
- [1] I. Žutić, A. Matos-Abiague, B. Scharf, H. Dery, and K. Belashchenko, *Mater. Today* **22**, 85 (2018).
 - [2] P. Lazić, K. D. Belashchenko, and I. Žutić, *Phys. Rev. B* **93**, 241401(R) (2016).
 - [3] I. Vobornik, U. Manju, J. Fujii, F. Borgatti, P. Torelli, D. Krizmanic, Y. S. Hor, R. J. Cava, and G. Panaccione, *Nano Lett.* **11**, 4079 (2011).
 - [4] S. Sakai, S. Majumdar, Z. I. Popov, P. V. Avramov, S. Entani, Y. Hasegawa, Y. Yamada, H. Huhtinen, H. Naramoto, P. B. Sorokin, and Y. Yamauchi, *ACS Nano* **10**, 7532 (2016).
 - [5] T. Chiba, S. Takahashi, and G. E. W. Bauer, *Phys. Rev. B* **95**, 094428 (2017).
 - [6] R. Watanabe, R. Yoshimi, M. Kawamura, M. Mogi, A. Tsukazaki, X. Z. Yu, K. Nakajima, K. S. Takahashi, M. Kawasaki, and Y. Tokura, *Appl. Phys. Lett.* **115**, 102403 (2019).
 - [7] J. Xu, S. Singh, J. Katoch, G. Wu, T. Zhu, I. Žutić, and R. K. Kawakami, *Nat. Commun.* **9**, 2869 (2018).
 - [8] M. N. Baibich, J. M. Broto, A. Fert, F. Nguyen Van Dau, F. Petroff, P. Eitenne, G. Creuzet, A. Friederich, and J. Chazelas, *Phys. Rev. Lett.* **61**, 2472 (1988).
 - [9] G. Binasch, P. Grünberg, F. Saurenbach, and W. Zinn, *Phys. Rev. B* **39**, 4828 (1989).
 - [10] S. Yuasa, T. Nagahama, A. Fukushima, Y. Suzuki, and K. Ando, *Nat. Mater.* **3**, 868 (2004).
 - [11] S. S. P. Parkin, C. Kaiser, A. Panchula, P. M. Rice, B. Hughes, M. Samant, and S.-H. Yang, *Nat. Mater.* **3**, 862 (2004).
 - [12] H. Nakayama, M. Althammer, Y. T. Chen, K. Uchida, Y. Kajiwara, D. Kikuchi, T. Ohtani, S. Geprägs, M. Opel, S. Takahashi, R. Gross, G. E. W. Bauer, S. T. B. Goennenwein, and E. Saitoh, *Phys. Rev. Lett.* **110**, 206601 (2013).
 - [13] Y.-T. Chen, S. Takahashi, H. Nakayama, M. Althammer, S. T. B. Goennenwein, E. Saitoh, and G. E. W. Bauer, *Phys. Rev. B* **87**, 144411 (2013).
 - [14] C. O. Avci, K. Garello, A. Ghosh, M. Gabureac, S. F. Alvarado, and P. Gambardella, *Nat. Phys.* **11**, 570 (2015).
 - [15] Steven S.-L. Zhang and G. Vignale, *Phys. Rev. B* **94**, 140411(R) (2016).
 - [16] K. Ganzhorn, J. Barker, R. Schlitz, B. A. Piot, K. Ollefs, F. Guillou, F. Wilhelm, A. Rogalev, M. Opel, M. Althammer, S. Geprägs, H. Huebl, R. Gross, G. E. W. Bauer, and S. T. B. Goennenwein, *Phys. Rev. B* **94**, 094401 (2016).
 - [17] D. Hou, Z. Qiu, J. Barker, K. Sato, K. Yamamoto, S. Vélez, J. M. Gomez-Perez, L. E. Hueso, F. Casanova, and E. Saitoh, *Phys. Rev. Lett.* **118**, 147202 (2017).

- [18] S. Cho, S. C. Baek, K.-D. Lee, Y. Jo, and B.-G. Park, *Sci. Rep.* **5**, 14668 (2015).
- [19] K. Yasuda, T. Morimoto, R. Yoshimi, M. Mogi, A. Tsukazaki, M. Kawamura, K. S. Takahashi, M. Kawasaki, N. Nagaosa, and Y. Tokura, *Nat. Nanotechnol.* **15**, 831 (2020).
- [20] K. Yasuda, A. Tsukazaki, R. Yoshimi, K. S. Takahashi, M. Kawasaki, and Y. Tokura, *Phys. Rev. Lett.* **117**, 127202 (2016).
- [21] Y. T. Chen, S. Takahashi, H. Nakayama, M. Althammer, S. T. B. Goennenwein, E. Saitoh, and G. E. W. Bauer, *J. Phys. Condens. Matter* **28**, 103004 (2016).
- [22] See Supplemental Material at <http://link.aps.org/supplemental/10.1103/PhysRevB.105.235202> for details of discussions and supplemental data.
- [23] K. Takiguchi, L. D. Anh, T. Chiba, T. Koyama, D. Chiba, and M. Tanaka, *Nat. Phys.* **15**, 1134 (2019).
- [24] N. T. Tu, P. N. Hai, L. D. Anh, and M. Tanaka, *Phys. Rev. B* **92**, 144403 (2015).
- [25] N. T. Tu, P. N. Hai, L. D. Anh, and M. Tanaka, *Appl. Phys. Lett.* **108**, 192401 (2016).
- [26] G. Wentzel, *Z. Physik* **38**, 518 (1926).
- [27] H. A. Kramers, *Z. Physik* **39**, 828 (1926).
- [28] L. Brillouin, *Comptes Rendus l'Académie Des Sci.* **183**, 24 (1926).
- [29] L. D. Zivanov and M. B. Zivanov, in *Proceedings of the International Semiconductor Conference, CAS* (IEEE, 1995), pp. 103–106.
- [30] P. Nam Hai, L. D. Anh, and M. Tanaka, *Appl. Phys. Lett.* **101**, 252410 (2012).
- [31] T. Jungwirth, W. A. Atkinson, B. H. Lee, and A. H. MacDonald, *Phys. Rev. B* **59**, 9818 (1999).
- [32] H. Zhao, J. Huang, Y. T. Chen, J. H. Yum, Y. Wang, F. Zhou, F. Xue, and J. C. Lee, *Appl. Phys. Lett.* **95**, 253501 (2009).
- [33] R. Suzuki, N. Taoka, M. Yokoyama, S. H. Kim, T. Hoshii, T. Maeda, T. Yasuda, O. Ichikawa, N. Fukuhara, M. Hata, M. Takenaka, and S. Takagi, *J. Appl. Phys.* **112**, 084103 (2012).
- [34] K. Takiguchi, L. D. Anh, T. Chiba, R. Fukuzawa, T. Takahashi, and M. Tanaka, [arXiv:2003.11731](https://arxiv.org/abs/2003.11731).
- [35] K. Sriharsha, L. D. Anh, N. T. Tu, S. Goel, and M. Tanaka, *APL Mater.* **7**, 021105 (2019).
- [36] R. P. Khosla and J. R. Fischer, *Phys. Rev. B* **2**, 4084 (1970).
- [37] S. Zhu, D. Meng, G. Liang, G. Shi, P. Zhao, P. Cheng, Y. Li, X. Zhai, Y. Lu, L. Chen, and K. Wu, *Nanoscale* **10**, 10041 (2018).
- [38] X. Liang, G. Shi, L. Deng, F. Huang, J. Qin, T. Tang, C. Wang, B. Peng, C. Song, and L. Bi, *Phys. Rev. Applied* **10**, 024051 (2018).
- [39] T. Takeda, S. Sakamoto, K. Araki, Y. Fujisawa, L. D. Anh, N. Thanh Tu, Y. Takeda, S. Fujimori, A. Fujimori, M. Tanaka, and M. Kobayashi, *Phys. Rev. B* **102**, 245203 (2020).
- [40] C. Gauer, J. Scriba, A. Wixforth, J. P. Kotthaus, C. R. Bolognesi, C. Nguyen, B. Brar, and H. Kroemer, *Semicond. Sci. Technol.* **9**, 1580 (1994).
- [41] K. Takiguchi, H. Shiratani, L. D. Anh, and M. Tanaka (unpublished).